ORIGINAL RESEARCH

Characterising the shear resistance of a unidirectional non-crimp glass fabric using modified picture frame and uniaxial bias extension test methods

K. D. H. N. Kahavita[1] · E. D. McCarthy[2] · M. Zhang[3] · C. M. Ó Brádaigh[2] · P. Harrison[1]

© Crown 2023

Abstract

The forming behaviour of a unidirectional non-crimp fabric (UD-NCF) consisting of polyamide stitches with a tricot-chain stitching pattern is explored. Notably, there are no stabilising tows orientated transverse to the main tow direction in this fabric, a common feature in many 'quasi' UD-NCFs, this allows extension of the stitch in the transverse direction under certain loading conditions. The lack of stabilising tows introduces a possible low-energy deformation mode to the UD-NCF, which is absent in biaxial fabrics and to a large extent in 'quasi' UD-NCFs. The in-plane shear behaviour is initially investigated using both standard 'tightly-clamped' picture frame tests and uniaxial bias extension tests. Preliminary results show a dramatic difference in results produced by the two test methods. During the picture frame test, fibres can be subjected to unintended tension due to sample misalignment in the picture frame rig. To mitigate error arising from this effect, the picture frame test procedure is modified in two different ways: by using an intentional pre-displacement of the picture frame rig, and by changing the clamping condition of test specimen. Results show that the modified picture frame test data contain less error than the standard 'tightly-clamped' test but also that the shear stiffness of the UD-NCF is notably lower when measured in the bias extension test compared to the picture frame test, mainly due to the difference in loading conditions imposed during the two tests.

Introduction

Fibre-reinforced plastics have seen increased deployment in a variety of industrial sectors such as aeronautics, automotive, and structural engineering, where high strength and stiffness with lightweight is required. Glass, carbon, and aramid fibres are all popular choices for the continuous fibre reinforcement phase due to their high strength-to-weight ratios and excellent chemical resistance [1]. Non-Crimp Fabrics (NCF) are currently receiving considerable interest in the academic literature due to their improved formability and in-plane mechanical properties (such as strength) when compared to woven fabrics due to the reduction of out-of-plane undulation (crimp) of the tows [2–4]. NCF is a type of engineering textile consisting of one (uniaxial/ unidirectional), two (biaxial) or many (multiaxial) aligned layers of differently oriented unidirectional layers of tows held together with a secondary thread [5, 6].

When designing an NCF, significant attention should be paid to its structure to improve both the mechanical properties and ease of handling and drapability over moulds of various shapes. The stitching in the NCF plays an important role in the fabrics drapability. It is typically made of polyester due to its excellent knitting properties (such as better tensile strength, flexibility, and tear resistance, which help to improve the properties in the direction of thickness by binding the unidirectional layers of tows together) and cost

✉ P. Harrison
  Philip.Harrison@glasgow.ac.uk

1   School of Engineering, University of Glasgow,
    Glasgow G12 8QQ, UK

2   The School of Engineering, Institute for Materials
    and Processes, The University of Edinburgh,
    Edinburgh EH9 3FB, UK

3   Johns Manville Technical Center, Johns Manville, 10100
    West Ute Avenue, Littleton, CO 80127, USA

effectiveness [7]. However, weak bonding between polyester yarns and matrix may cause failure in the composite [8]. In some studies, polyester stitches are replaced with polyethylene [9, 10] stitches or structural fibres such as E-glass [11–13] to improve fabric properties. Using matrix-soluble stitching materials with low melting points, such as polyamide and phenoxy, rather than polyester yarns, can improve the mechanical properties of composites [14]. The properties of the stitching material are essential in developing a suitable NCF for its final application. There are different types of stitching patterns (e.g., chain, tricot, and tricot-chain) that can be used to control the formability of the NCF. Generally, chain stitching can improve the drape quality, while tricot stitching enhances the stability (or reduces the pre-shear) of the fabric. Optimal combination of these two patterns can balance the drape and stability properties [14].

Sheet forming is one of the most promising, low-cost manufacturing techniques for advanced composite materials [15–17]. The deformation mechanics of a material can significantly influence the success of the forming process for a given component geometry [18]. The final fibre orientations, and the presence of defects such as wrinkles [19, 20], tears [21] and fibre waviness [22], induced during the forming process, all affect the mechanical properties of the final product [23]. Consequently, a good understanding of the fabric's mechanics during forming can help improve the efficiency and productivity of the manufacturing process, and simulation of the forming process has proven to be an important tool for cost reduction and process optimisation [24]. The development of macroscale constitutive models [24–26] to describe the forming behaviour of engineering fabrics is typically informed by experimental analysis [27–29], though attempts have also been made to predict the properties using multiscale modelling approaches [30–32].

When compared to biaxial engineering fabrics, the experimental and numerical analysis of the forming behaviour of unidirectional-NCF is limited. Most previous experimental investigations into the formability of UD-NCFs, e.g. [9–11, 33–38] have considered fabrics that are not purely unidirectional and do in fact, contain a small weight fraction of glass fibre tows, orientated transverse to the main fibre direction, incorporated to stabilise the fabric during forming (referred to as quasi-UD-NCFs by Vallons et al. [39], a terminology adopted throughout this paper). Despite their relatively minor influence on a composite part's final mechanical properties, the relatively high stiffness of these stabilising tows (compared to the stitch stiffness) means that they can play a significant role in the fabric's forming behaviour [9]. The in-plane shear and out-of-plane bending of quasi-UD-NCFs was experimentally investigated in [9–11, 33–38]. The in-plane shear behaviour is often found to be asymmetrical with respect to the shear direction, because of the position and orientation of the stitching. The influence of the stabilising tows on formability depends on several factors, including the degree of attachment of the stabilising tows to the rest of the fabric; a looser coupling allows for more intraply slip, potentially leading to 'ambiguous' mechanical behaviour [9]. Despite the interest in quasi-UD-NCFs, the forming mechanics of purely UD-NCFs, i.e. those that use only stitching to stabilise the fabric and have no additional stabilising transverse glass-fibre tows stitched to the back of the fabric have received relatively little attention [40, 41]. This work addresses this point.

Material

A UD-NCF supplied by Johns Manville is investigated. It has a tricot-chain stitching pattern, with chain stitches running along the front of the fabric (perpendicular to the tow direction, typically resulting in symmetric shear behaviour [42]), and tricot stitches running across the back (see Fig. 1). The warp direction of the fabric contains glass fibre

Fig. 1 Close-up images of unidirectional tricot-chain stitched non-crimp glass fabric surface (**a**) front (**b**) back. Small increments on bottom scale in mm
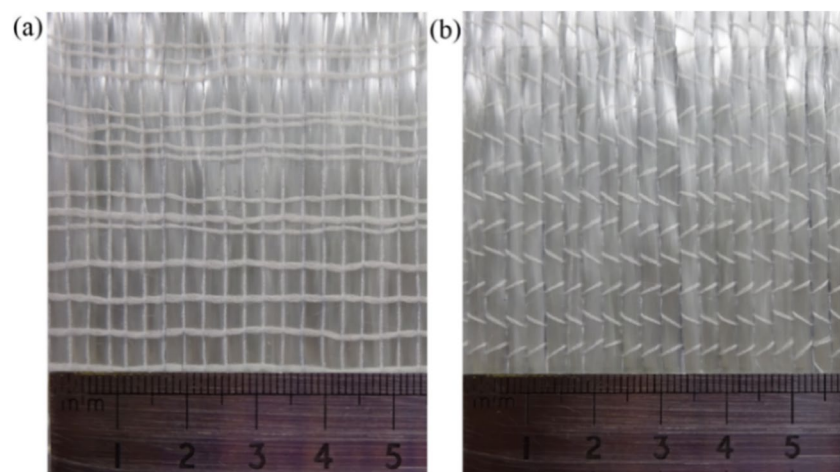
tows (Johns Manville StarRov® 886—2400 tex) with a width of 2.63 ± 0.16 mm (error signifies ± 1SD), while the weft direction contained stitches (67 dtex) with a width of 0.55 ± 0.05 mm. The widths of the tows and stitches were measured using ImageJ software [43]. The thickness of UD-NCF is approximately 1 mm and the areal density of the fabric is 1370 ± 14 g/m^2. The stitches are made of polyamide (PA 6.6) and are extensible with a low tensile stiffness. The use of a compliant stitch material allows for significant stretching along the chain direction of the stitch pattern perpendicular to the main tow direction, introducing an additional low-energy deformation mode for the UD-NCF. This mode of deformation can become important during complex forming operations, depending on the forces applied to the fabric and the layup used in the blank.

Preliminary investigation

A preliminary investigation of the in-plane forming mechanics of the UD-NCF was conducted using both the Uniaxial Bias Extension (UBE) [24] and Picture Frame (PF) [44] tests, see Fig. 2. Both these tests have been used to characterise the shear behaviour of biaxial engineering fabrics [45, 46], quasi-UD-NCFs [9, 11] and to some extent UD-NCFs [40]. A Zwick Z2 electromechanical test machine fitted with a 2kN loadcell was used for both. All tests were repeated 4 times and the error bars indicate ± 1SD.

A well-lubricated, low friction PF rig with 170 mm side length was used, the standard test procedure is described in the Section 'Standard Tightly-Clamped Picture Frame Test'. The other shear test, the UBE test, is a tensile test performed on a rectangular-shaped fabric specimen with the tows and stitches initially oriented at $\pm 45°$ to the direction of applied tensile force, see Fig. 2a. In this investigation, the tested specimen area measured 400×200mm^2. Following [24], aluminium foil was bonded to both the clamping region and 'Region C' (see Fig. 2a) to allow easier drilling of holes and to mitigate intra-ply slip. For biaxial woven fabrics, the shear stiffness of the fabric can be determined from the UBE test results using appropriate theoretical analysis. The assumption in this type of analysis is that the specimen undergoes trellis shear kinematics (just pure shear, with no extension of the fibres in the warp and weft directions and no resistance to in-plane bending), the fabric response is rate-independent, and the shear stiffness is purely a function of the shear angle [10] (though this latter assumption can be extended to include more complex behaviour [29, 47]).

Typically, for most biaxial woven fabrics, after normalisation (by the side length of Region A or L_A shown in Fig. 2a for UBE test and by the side length of the rig for PF test), the shear results of these two tests on the same fabric are expected to be reasonably close (assuming no misalignment errors, which in practice can be considerable and difficult to avoid). The UBE test should produce a slightly higher normalised axial force (by a few percent, due to the 'extra' force contribution of fabric in Region B, see Fig. 2a), though after analysis of the different deformations induced by the two tests, the shear resistance of biaxial woven fabrics extracted from the two tests, should be about the same [10].

Turning now to prior investigations dealing with quasi-UD-NCFs, at low shear angles, a comparison of the normalised forces measured using the PF and UBE tests by both Schirmaier et al. [9] and Ghazimoradi et al. [11], reveals that the two test methods produced results that matched to within around 20% at low shear angles. However, as the shear angle increased (beyond about 35° in Ghazimoradi et al. [11]), the measurements of the two test methods diverged, due to the changing kinematics and loadings applied to the different

Fig. 2 Two different shear tests (**a**) standard UBE test (400*200mm^2), Region A is denoted by the yellow square in the figure (**b**) standard tightly-clamped PF test (170*170mm^2), green and blue arrows indicate the initial chain-stitch direction (green) and the tow (blue) directions
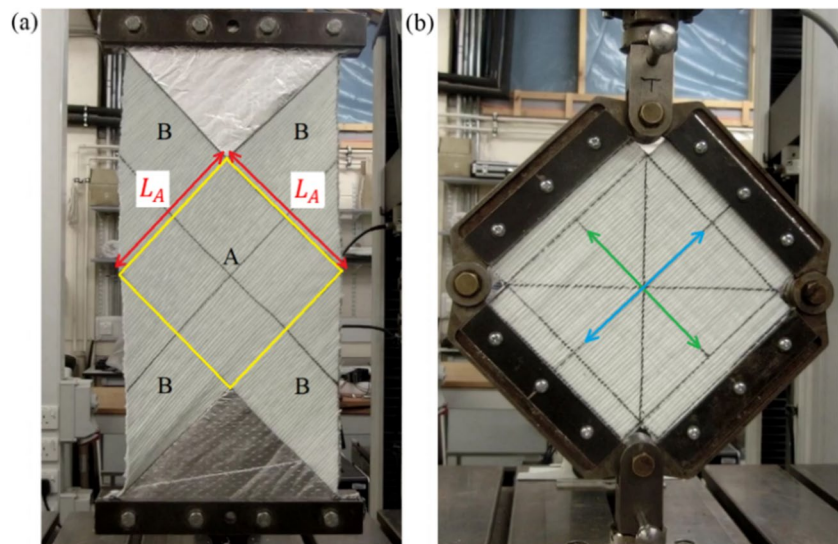
types of specimens. The divergence was so great that Schirmaier et al. [9] concluded that the 'picture frame test is not suitable to characterise the shear deformation behaviour of UD-NCF', as the imposed deformations were considered too far removed from those experienced during actual forming situations. Here we take the view that the PF test can be useful in accessing extreme types of deformation, available to the fabric given the right forming conditions, e.g. if the blank is comprised of multiple sheets of initially orthogonal UD-NCF plies. Although, when using the PF test, one must be very careful to ensure that the test is measuring the

desired 'signal' resulting from fabric shear, rather than the unwanted 'noise' associated with tensions induced by specimen misalignments (see Launey et al. [45]).

Figure 3 compares the normalised force from the UBE test (axial force divided by L_A as shown in Fig. 2a) and the PF test (axial force divided by the side length of the rig) versus measured shear angle curves on the UD-NCF considered in this investigation. Manual image processing (using ImageJ software [43]) was used to measure the shear angle at a given displacement during the test which is determined by the difference between the initial tow-stitch angle (see Fig. 2b – angle between green and blue arrows) and the tow-stitch angle at a given displacement. The front of the experiments was captured with a Casio EX-ZR700 digital camera. The results reveal an unusual forming response, which motivated much of the work presented in subsequent sections. In particular, the UD-NCF shows a dramatically lower normalised force when tested in the UBE test compared to the force measured by the PF test, especially at low shear angles (at 5˚ the PF test result is 16 times higher, at 10˚ it is 10 times higher and at 30˚ it is about 3 times higher than UBE test—see Fig. 3). This difference in the results generated by the two test methods is notably greater than that reported by either Schirmaier et al. [9] or Ghazimoradi et al. [11] and merits further investigation.

Figure 4 compares the two test specimens at a shear angle of 25°. The kinematic behaviour of the UBE test (see Fig. 4a) is asymmetric, in contrast to the symmetric deformation of the PF test (see Fig. 4b). Stitch extension is clearly visible when comparing the side lengths of Region A (L_A) in the undeformed and deformed UBE specimens. L_A
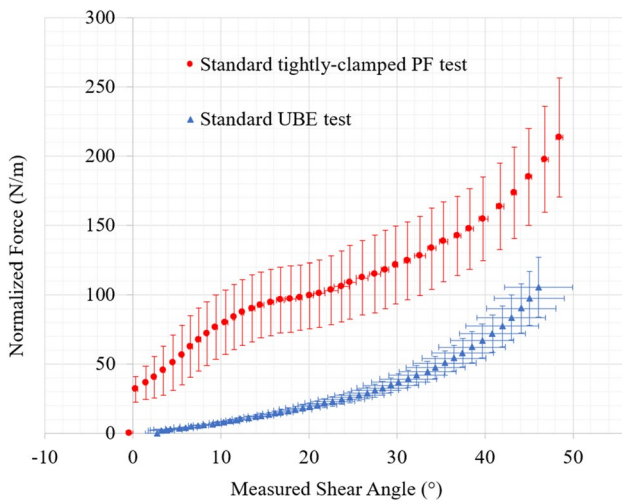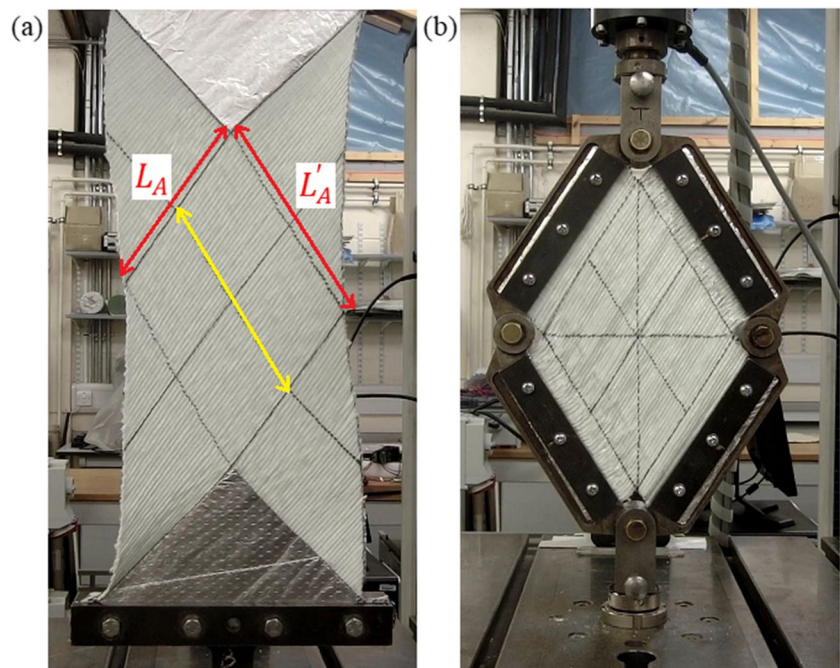

Fig. 3 Comparison of normalized force vs measured shear angle curves of standard tightly-clamped PF and UBE tests for UD-NCF

Fig. 4 UD non-crimp glass fabric specimens at the shear angle of 25° (**a**) Standard UBE test (yellow arrow indicates the direction of stitch strain) (**b**) standard tightly-clamped PF test

is approximately the same on both sides of the undeformed specimen (see Fig. 2a). During deformation, the value of L_A along the stitch direction (L_A') increases due to the stitch strain (see Fig. 4a). Ghazimoradi et al. [11] described similar kinematics during their UBE tests on a quasi-UD-NCF specimen (see their Fig. 2). Schirmaier et al. [9] also reported unusual kinematics in their UBE tests, with their test specimen vaguely resembling the shape of Region A in Fig. 4 (see their Fig. 8), but with less homogeneity in the strain field.

The degree to which quasi-UD-NCFs (containing stabilising tows) follow these alternative asymmetric kinematics (shown in Fig. 4), no doubt depends on the cohesion and integrity of the fabric, itself determined by the specimen size, and the strength of the connection between the stabilising tows and the rest of the sheet. The looser the connection, the greater the ability of the stabilising tows to 'slip', and the closer the main tows in the sheet can follow the asymmetric kinematics shown in Fig. 4 (see Fig. 2 in Ghazimoradi et al. [11] and Fig. 3 in Krogh et al. [35]). The heterogeneity in the strain field reported by Schirmaier et al. [9] suggests that the strength of the connection between the stabilising tows and the rest of the fabric may sometimes vary across the fabric, leading to inconsistent and irregular shear kinematics. When testing quasi-UD-NCFs, to limit slip between the stabilising tows and the rest of the sheet Krogh et al. [35] suggested the use of either large test specimens (to improve fabric integrity) or, more conveniently, the use of an alternative 'diamond' specimen geometry together with anti-wrinkle plates. The latter allowed the measurement of pure shear (no slip) kinematics up to 45°. Whether one should aim to limit intraply slip [35] or allow it to occur [9]; [11] in characterisation tests is debatable. A full understanding of the forming behaviour of quasi-UD-NCFs may require both. In this current investigation, because no stabilising tows are present (the fabric is a UD-NCF, not a **quasi**-UD-NCF), there is no intraply 'slip' and no tendency towards pure shear kinematics with increasing specimen size, and so without stabilising tows, the asymmetric UBE test kinematics shown in Fig. 4 are inevitable, no matter the sample size or shape [10].

Returning to the force measurements in Fig. 3, this very large discrepancy between the PF and UBE test results, especially at low shear angles, presents a puzzle with two possible explanations; the difference in behaviour could be due to: (*a*) *experimental error* (fibres are more likely to be subjected to unintended tension during the PF test due to accidental misalignment when loading the specimens) *or (b) there is a real and very large change in the shear resistance of the fabric when subject to the two different types of test condition.* If so, then this behaviour would ideally be incorporated in the formulation of constitutive models and should therefore be properly understood. This paper focuses on simple modifications of the typical PF test to overcome potential experimental errors and more fully explore option (a).

Examination of error in preliminary picture frame test results

The PF test is notoriously susceptible to error due to specimen misalignment that can result in an overestimate of the fabric's shear stiffness [45]. When loading the specimen in the PF rig, it is important to keep the tows aligned with the side of the rig. Misalignment produces unwanted tensile or compressive strains along the tow directions (see Fig. 5). Tensile strain prevents the specimen from wrinkling, but it can lead to significant force overestimations while compressive strains induce wrinkles at low shear angles, making accurate measurement of the specimen shear angle problematic [48].

In the literature, various PF test procedures have been proposed with several suggested variations around the boundary conditions of the test, the decision to use a tightly-clamped or a lightly clamped boundary condition has often been discussed [46, 49]. In some of the earliest tests, McGuiness and Ó Brádaigh [50, 51] advocated the use of a lightly-clamped pinned boundary condition to reduce misalignment errors and to facilitate rotation of the fibres under clamps to minimise fibre kinking [49, 52], recognising that the in-plane bending stiffness of the fibres [24] would otherwise create an s-shaped fibre direction, complicating the shear kinematics and creating unwanted tension in the fibres. Lebrun et al. [46, 49] used a tightly-clamped boundary condition with both a regular and an alternative-shaped test specimen geometry, the latter had a significantly reduced clamping area producing much lower forces than the regular shaped specimen; though both sets of results still contained great variability. Harrison et al. [44] used both tightly and lightly clamped
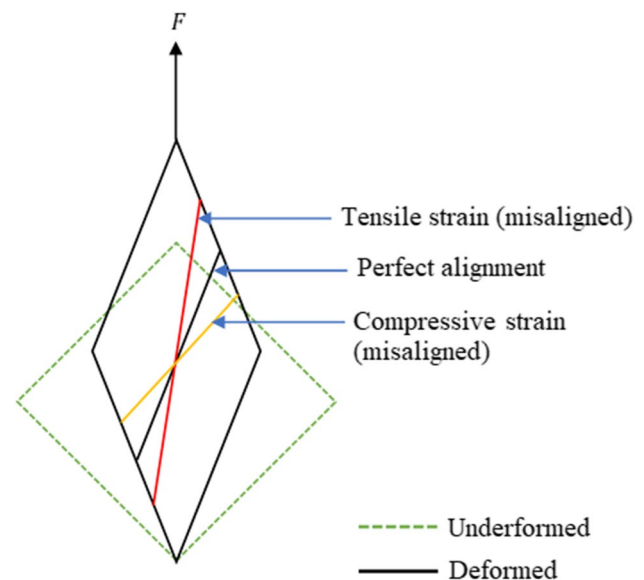

Fig. 5 Types of misalignments of the tows in the PF test

(pinned) boundary conditions; a tight clamping condition was required to impose shear across a relatively stiff room temperature carbon/epoxy prepreg while a light clamping was sufficient to shear a low-stiffness glass/thermoplastic fabric. All the groups involved in the benchmarking investigation reported in Cao et al. [53] used a tightly clamped boundary condition (the scatter between the reported PF results was very high), as did Lomov et al. [54] who explored the consequences of tight clamping on the sample's full field shear kinematics. Launay et al. [45] devised an instrumented PF rig in which the clamping system was connected to the PF via two load sensors. During the test, the tension of the yarns was measured and adjusted. Rubber strips under the clamps were examined in [9] and needle gripping of the folded ends of the specimen was examined in [55, 56]. To reduce the in-plane bending and shear stiffness near the specimen's edge region, removal of the transverse yarns in the specimen 'arms' was suggested [55, 57]. These modifications are not suitable for UD-NCFs because the fibres are aligned along the warp direction and the stitches are in the weft direction (low stiffness compared to glass tows), which may prevent the uniform deformation of the sample during the PF tests. A 'needle-integrated frameless' PF test suitable for commingled polypropylene/glass fabrics was devised with the inclusion of a sensor in [58]. Other researchers attempted to reduce misalignment error by mechanically pre-conditioning the PF test specimens (by shearing the sample several times up to a moderate shear angle) [53, 59]. This method helps to overcome the misalignment by stretching the fibres. However, in practise, this form of preconditioning is contentious because the change in the meso-structure of the specimen caused by preconditioning is not representative of the unconditioned specimen. Krishnappa et al. [60] used a PF setup with a pre-tensioning apparatus to overcome both alignment and clamping issues. In this investigation, two relatively simple modifications to the standard PF test method have been employed to examine the possibility of an overestimated shear force measured in

the PF test. The results are compared with those measured using the standard tightly-clamped PF test.

Standard tightly-clamped (Bolted) picture frame test

Figure 6a shows the PF rig, which is made up of four identical bars that are hinged together by bearings. Four samples were prepared from the glass UD-NCF, based on the standard dimensions (see Fig. 6b). To improve handling during drilling of the bolt holes, four aluminium foils were adhered to each side of the clamping area. The samples were then bolted in the rig (aligned as precisely as possible) with a high torque, resulting in a rigid boundary condition. The PF tests were performed on a Zwick Z2 tensile testing machine mounted with a 2kN load cell. The strain rate was set to 1 mm/s with a maximum upper force limit of 1000N, and the standard force and travel (displacement) were recorded.

Two cameras were used to film the tests, one in front to measure the shear angle at known displacements and one behind to detect the onset of wrinkling. Understanding the development of wrinkles is important as it can dramatically reduce the mechanical properties of the specimen and the reliability of the test results. It has been found that wrinkling can introduce a substantial overestimation of the measured shear angle when using manual image analysis to interpret the test results (by up to 20%) [62]. Although the occurrence of wrinkling is often considered as a source of the UBE test error, the wrinkling onset angle can also be used to analyse the mechanical properties (torsional rigidity) of a sheared fabric [27]. A horizontal line was marked on the back of the specimen (across the midsection) for the post examination of the wrinkling onset. When the tensile force is applied to the specimen, the horizontal line tends to deform at a certain time. The wrinkle onset angle was then determined using the corresponding front still frame (by splitting the videos using VitualDub [63]) obtained from the time-synchronized

Fig. 6 (**a**) Schematic of a PF shear rig [61] (**b**) Prepared PF test specimen
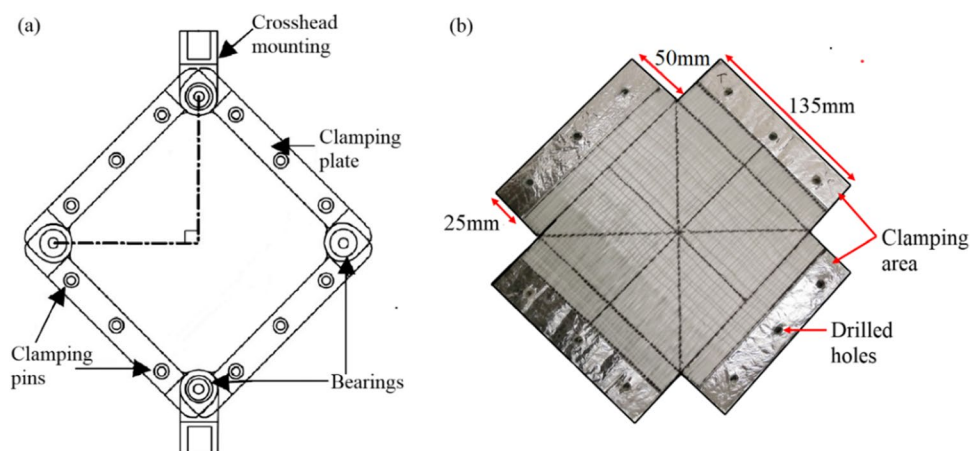
front camera. Manual image processing (i.e., ImageJ [43]) was used to measure the shear angle at a given displacement during the test. The shear angle measured at that point determines the wrinkle onset angle.

When pulling the PF diagonally in one direction, the square shape of the frame transforms into a rhomboid (see Fig. 7a). Based on the test geometry change (see Fig. 7b), the fabric shear angle θ, can be directly related to the displacement of the crosshead, d_{pf}, using the Eq. (1),

$$\theta = \frac{\pi}{2} - 2acos\left[\frac{1}{\sqrt{2}} + \frac{d_{pf}}{2L_{pf}}\right] \tag{1}$$

where, L_{pf} is the side length of the PF rig. The shear angle,θ, can be determined by the difference between the initial frame angle (90°) and frame angle, $2\emptyset$, at a given displacement.

$$\theta = \left(\frac{\pi}{2}\right) - 2\emptyset \tag{2}$$

For the PF test, the fabric's shear resistance is expressed as.

$$F_s = \frac{F_{af}}{2L_{pf}cos\emptyset} \tag{3}$$

where, F_{af} and F_s represent the total axial force and the normalised shear force per unit length, respectively [53].

Pre-displaced tightly clamped picture frame test

The first modification of the standard, tightly-clamped (bolted) PF test procedure considered in this study is a simple technique designed to reduce sensitivity to inevitable sample misalignment in the PF test by pre-displacing the PF rig, prior to loading the specimen (which is unsheared, i.e., with 0° of shear). There are two methods of pre-displacing the rig, namely, positive, and negative. Figure 8b shows positive pre-displacement of the rig by moving the rig upward. Figure 8c shows negative pre-displacement by moving the rig downward. For the PF rig used in this investigation, which has a side length of 170 mm, two different initial positive displacements, 4 mm and 6 mm, were used. The initial displacement can be expressed as a fraction of the PF side length to obtain the 'normalised pre-displacement'. Therefore, the normalised initial displacements are 0.0235 (4/170) and 0.0353 (6/170), corresponding to an initial rig shear angle of about 2° and 3°, respectively. Rig shear angle is defined as the difference between initial frame angle of the standard PF test (90˚—see Fig. 8a) and the initial frame angle of the pre-displaced test.

The analysis assumes that the specimen can be loaded into the pre-displaced rig while maintaining the initial tow-stitch angle at 90˚. The idea behind the pre-displaced PF rig method is to minimise misalignment error by intentionally inducing compressive stress in the fibre directions during the test. Care must be taken with pre-displacement values because high values can introduce unwanted buckling in the fibres. The maximum initial displacement that could be used in this investigation without affecting the original dimensions of the specimen's region of interest (i.e., shear region) was found to be 6 mm (though to fix the specimen to the PF rig without deforming it, the edges of the clamping area had to be trimmed slightly). When compared to the side length of the rig, this value is low (the normalised pre-displacement is 0.0353). Based on this method, the theoretical axial engineering strain of the fibres versus tow shear angle was determined (assuming the tows are perfectly clamped in the
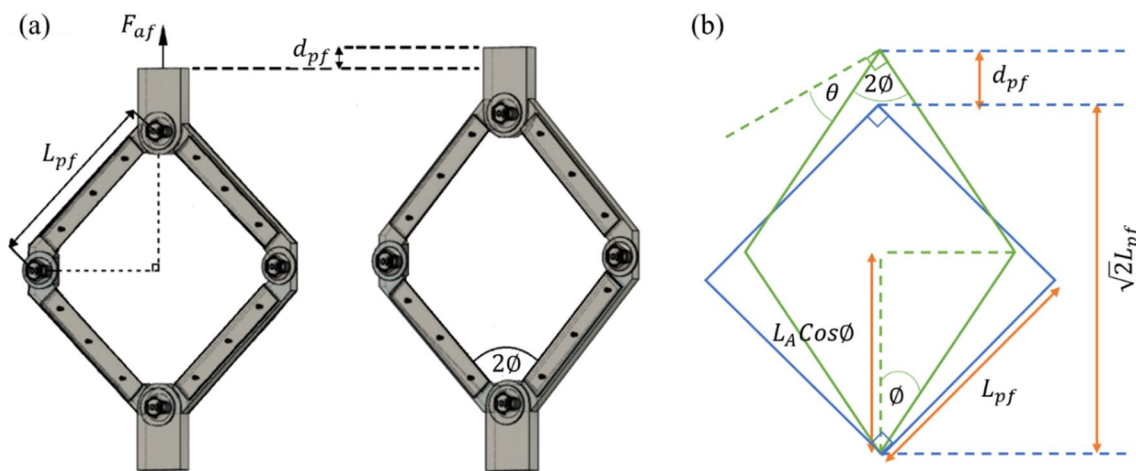

Fig. 7 (**a**) Displacement of the PF test (**b**) Geometry change of the PF specimen
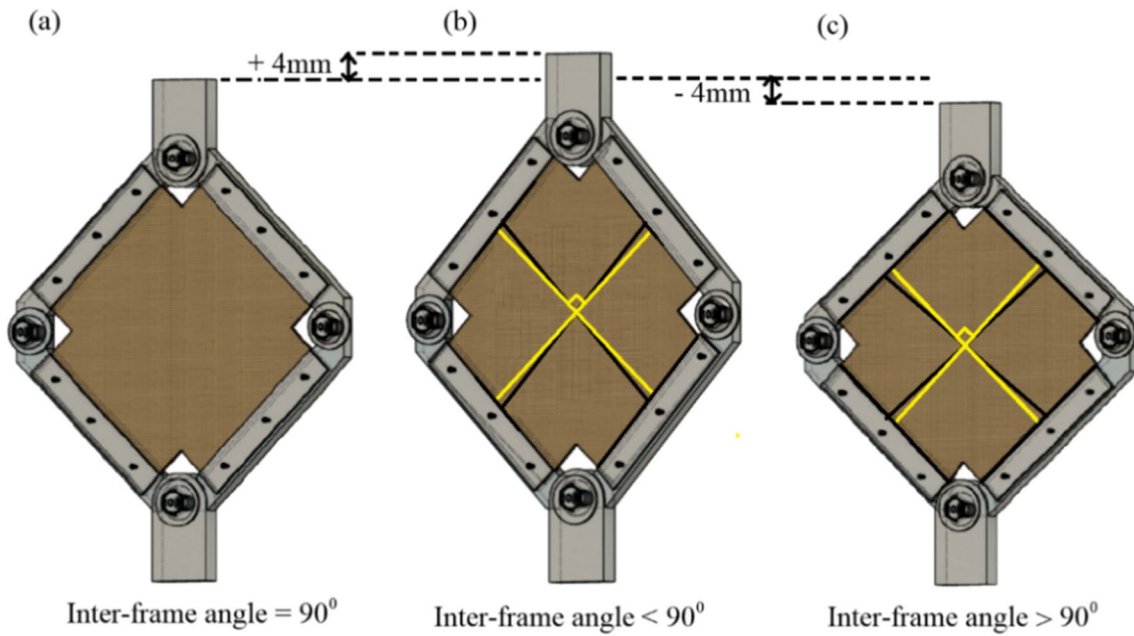
Fig. 8 (**a**) Standard PF rig (**b**) Positive pre-displaced rig (**c**) Negative pre-displaced rig (the angle between the two black lines represents frame angle and the angle between two yellow lines represents the initial tow-stitch angle)
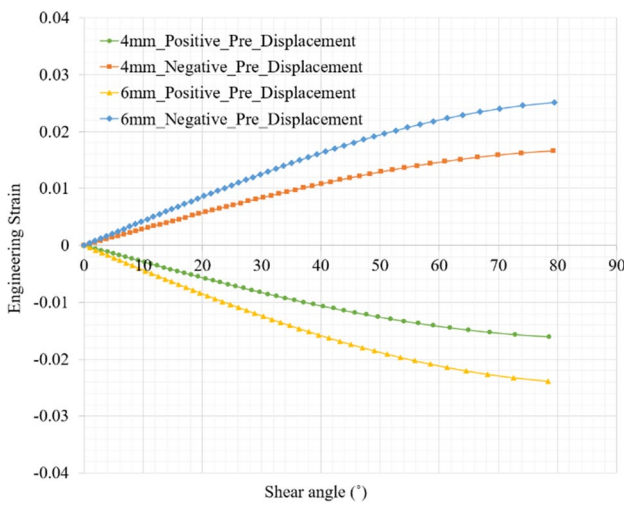

Fig. 9 Shear angle vs engineering strain curves of positive and negative pre-displaced PF rig for a relative initial displacement of ± 4 mm and ± 6 mm, corresponding to an initial rig shear angle of approximately 2° and 3°, respectively

PF rig). The theoretical tow shear angle vs axial engineering strain predictions, corresponding to positively and negatively pre-displaced PF rigs, are shown in Fig. 9. Here ε_p and δ_p represent the engineering strain and the theoretical tow shear angle of the positively pre-displaced PF rig respectively and are given in Eqs. (4) and (5), see Appendix A and Appendix

B for derivation. ε_n and δ_n represent the engineering strain and theoretical tow shear angle of the negatively pre-displaced PF rig respectively and given are in Eqs. (6) and (7), see Appendix C and Appendix D for the derivation.

$$\varepsilon_p = \frac{\left\{ \frac{d_1 \sin\theta_2 + \left[\frac{L_{pf}}{2}\right]\sin\theta_2}{\sin\left(\tan^{-1}\left[\frac{(\tan\theta_2)(2d_1 + L_{pf})}{L_{pf} - 2d_1}\right]\right)} \right\} - \left\{ \sqrt{2}\left(\left[\frac{L_{pf}}{2}\right]\cos\theta_1 - \frac{\left[\frac{L_{pf}}{2}\right]\cos\theta_1(\cos\theta_1 - \sin\theta_1)}{\cos\theta_1 + \sin\theta_1}\right)\right\}}{\left\{ \sqrt{2}\left(\left[\frac{L_{pf}}{2}\right]\cos\theta_1 - \frac{\left[\frac{L_{pf}}{2}\right]\cos\theta_1(\cos\theta_1 - \sin\theta_1)}{\cos\theta_1 + \sin\theta_1}\right)\right\}} \quad (4)$$

$$\delta_p = \frac{\pi}{2} - 2\tan^{-1}\left\{ \frac{\tan\left(a\cos\left[\frac{1}{\sqrt{2}} + \frac{D}{2L_{pf}}\right]\right)(2d_1 + L_{pf})}{L_{pf} - 2d_1} \right\} \quad (5)$$

where, θ_1 and θ_2 represent the initial frame angle and the frame angle at a given displacement (see Eq. (10) and Eq. (15) Appendix A) in the positive pre-displaced PF rig test. L_{pf} is the side length of the PF rig, and d_1 is a constant that depends on the amount of pre-displacement (see Eq. (19) Appendix A). D is the displacement of the machine crosshead at a given time.

$$\varepsilon_n = \frac{\left\{ \frac{\left(\left[\frac{L_{pf}}{2}\right]\sin\theta_2' - d_1'\sin\theta_2'\right)}{\sin\left(\tan^{-1}\left[\frac{(\tan\theta_2')(L_{pf} - 2d_1')}{L_{pf} + 2d_1'}\right]\right)} \right\} - \left\{ \sqrt{2}\left(\left[\frac{L_{pf}}{2}\right]\cos\theta_1' + \frac{\left[\frac{L_{pf}}{2}\right]\cos\theta_1'(\sin\theta_1' - \cos\theta_1')}{\sin\theta_1' + \cos\theta_1'}\right)\right\}}{\left(\sqrt{2}\left(\left[\frac{L_{pf}}{2}\right]\cos\theta_1 - \frac{\left[\frac{L_{pf}}{2}\right]\cos\theta_1(\cos\theta_1 - \sin\theta_1)}{\cos\theta_1 + \sin\theta_1}\right)\right)}$$

$$(6)$$

$$\delta_n = \frac{\pi}{2} - 2\tan^{-1}\left\{\frac{\tan\left(acos\left[\frac{1}{\sqrt{2}} + \frac{D'}{2L_{pf}}\right]\right)\left(L_{pf} - 2d_1'\right)}{L_{pf} + 2d_1'}\right\}$$

(7)

where, θ_1' and θ_2' represent the initial frame angle and the frame angle at a given displacement (see Eq. (27) and Eq. (32) in Appendix C) in the negative pre-displaced PF rig test. d_1' is a constant that depends on the amount of pre-displacement (see Eq. (36) Appendix C). D' is the displacement of the machine crosshead.

The negative pre-displaced method shows positive engineering strain in the tow direction, which increases the force required to extend the PF rig due to increased tow tension. In contrast, the positive pre-displaced method produces negative axial engineering strain with increasing shear angle. Therefore, the fibres are compressed (or more likely, buckle) in the positive pre-displacement method. As a result, the axial tensile strain of the tows/fibres becomes compressive when the rig is pre-displaced in the positive direction, mitigating against any unintended fibre tension due to accidental sample misalignment.

Four samples were prepared for each of the positive pre-displaced tightly-clamped PF tests (i.e. 4 mm and 6 mm initial positive pre-displacements). The specimens were bolted in the positive pre-displaced rig resulting in the same edge condition as the standard tightly-clamped test while maintaining the initial tow-stitch angle of the specimens at 90°. The tests were performed on the same tensile testing machine as the standard method. Based on the test geometry change, the theoretical tow shear angle of the positive pre-displaced PF test (δ_p) can be calculated as Eq. (5) (see Appendix B for derivation).

Low & high pressure clamped picture frame test using G-clamps

In this second simple method, rigid bolting of the specimen was replaced by G-clamps with two different tightening pressures (low and high – corresponding to the torque of 1Nm and 5Nm, respectively) to determine how the clamping condition affects the measured force (see Fig. 10a). Note that here 'high' pressure clamping imposed by the G-clamps is still expected to produce a significantly lower clamping pressure than the 'tight' clamping condition imposed when using bolts. This method is also used by Schirmaier et al. [9], Ghazimoradi et al. [11] and Senner et al. [40] though the clamping pressure used in those investigations is not specified. The clamping technique does not require the use of aluminium foil or drilling of the samples (for bolt holes). To distribute pressure evenly, eight silicon rubber strips were placed on either side of the sample underneath the clamps (see Fig. 10b). The tests were performed in the Zwick Z2 tensile testing machine using the same testing parameters as used in the tightly-clamped, standard and positive pre-displaced PF tests.
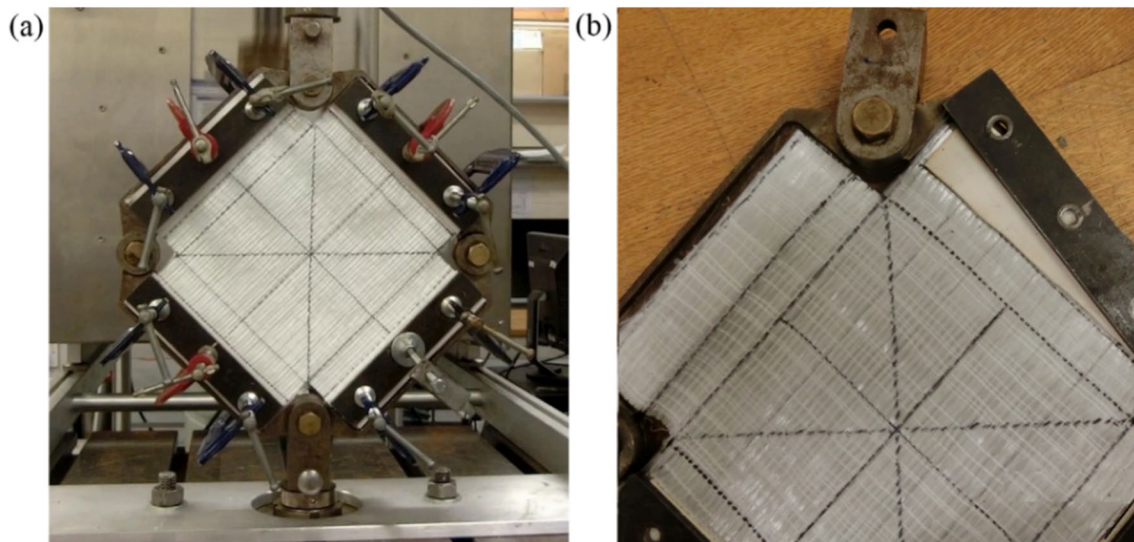

Fig. 10 PF test setup with G-clamps rather than using bolts (**a**) front view (**b**) showing positioning of rubber strips under the clamps to more evenly distribute pressure
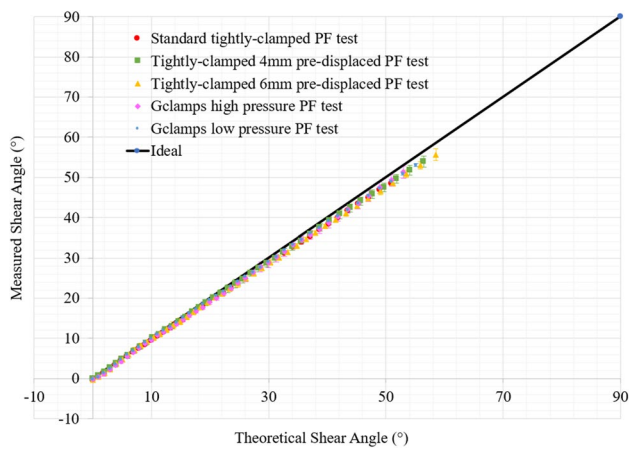
**Fig. 11** Comparison of average measured vs theoretical shear angle curves of all PF tests

Results and discussion

Figure 11 depicts the average curves of the measured shear angle versus the theoretical shear angle in reference to the ideal curve (i.e., assuming that the fibres are inextensible [29]). The image analysis method was used to determine measured shear angles at various crosshead displacements, and the theoretical shear angle was calculated using Eq. (1) for the standard and G-clamped PF tests, and Eq. (5) for the 4 mm and 6 mm pre-displaced PF tests. The PF test assumes pure deformation within the specimen. All the averaged curves overlap and are close to the ideal curve. However, at high shear angles, the results show a minor deviation below the ideal line, probably due to the presence

of wrinkles, which reduces the reliability of the shear angle measurements.

The normalised shear force, calculated using Eq. (3), versus measured shear angle response for each modified PF test was compared with the result from standard PF test, as shown in Fig. 12 (the error bars on the points represent ± 1 standard deviation). All the PF tests were 'zeroed', and the force curves consequently begin at (0,0). An abrupt increase in normalised shear force is observed at the beginning of shear in the PF results (see Figs. 3 and 12). The reason for this load 'jump' is not entirely clear (tests with other materials in the PF rig showed no such jump, ruling out friction of the PF rig during loading as the cause). This abrupt jump in the normalised shear force is notably absent in prior investigations on quasi-UD-NCFs [9, 11, 34, 37]. It is also absent in the UBE tests in this study (see Fig. 3), perhaps because the UBE test specimen is free to immediately stretch along the stitch direction at the start of the test, or maybe due to the free edges of the specimen allowing relaxation of possible stitch tension as discussed by Senner et al. [40]. All modified PF tests show lower normalised shear force data when compared to the standard tightly-clamped PF test result, with a smaller jump at the start of the tests. The 4 mm pre-displaced tightly-clamped method shows a modest reduction compared to the standard tightly-clamped method at low shear angles (less than 25°), this reduction is noticeable only at low shear angles but becomes insignificant at higher shear angles (above 25°). In contrast, the 6 mm pre-displaced tightly-clamped method shows a much larger reduction, even to high shear angles. The pre-displaced results show that the rig's initial displacement has a significant influence on the measured shear stiffness

Fig. 12 Comparison of Normalized force vs measured shear angle average curves of all PF tests
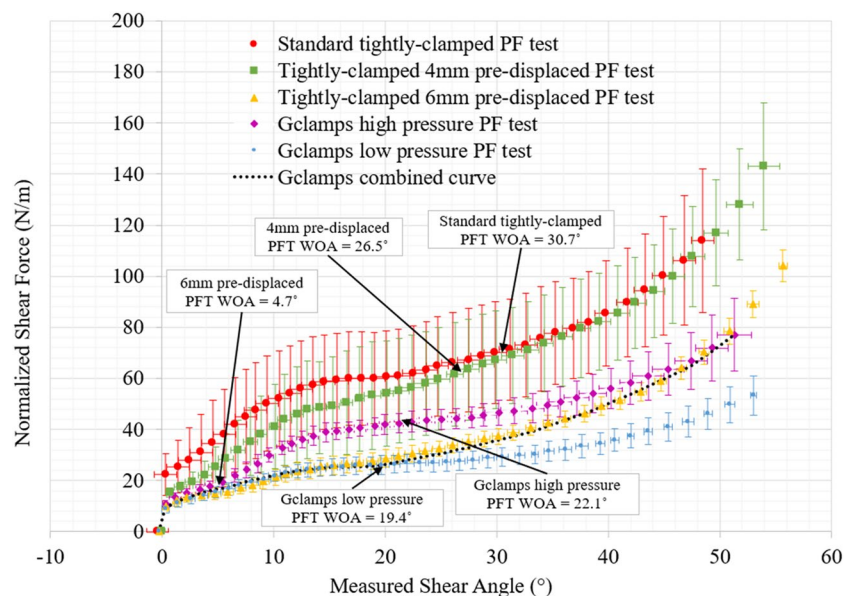
of the specimen. Presumably this is because the compression induced along the tow direction with increasing shear angle reduces any tow tension caused by random sample misalignments and in-plane fibre bending [51]. Corroborating this idea, the average Wrinkle Onset Angle (WOA) of the 6 mm pre-displaced results (an effective proxy measure of compressive stresses in the sheet) moves to lower shear angles (4.7°) compared to the 4 mm pre-displaced method (26.5°) and the standard PF test (30.7°).

Note that the wrinkles tend to occur along the stitch direction rather than the tow direction, facilitated by the very low out-of-plane bending stiffness of the sheet in this direction (as opposed to in the tow direction, which has a much higher out-of-plane bending stiffness, resisting the low-wavelength buckles evident in Figs. 13 and 14). In addition to serving as an indicator of low misalignment tensile stresses, wrinkling can provide a lower-energy (and therefore lower force) mode of deformation for the specimen during the test as it results in less in-plane compression and shear. It may

Fig. 13 Wrinkling behaviour of G-clamps PF test specimens at 35° shear angle (a) high-pressure G-clamp (b) low-pressure G-clamp
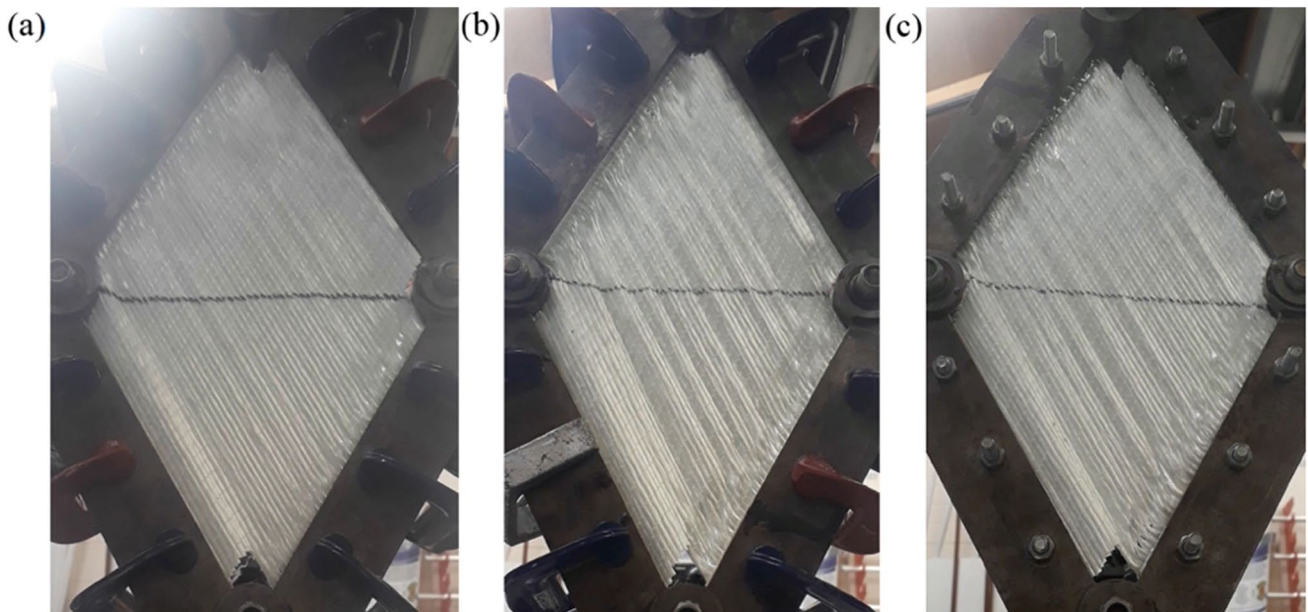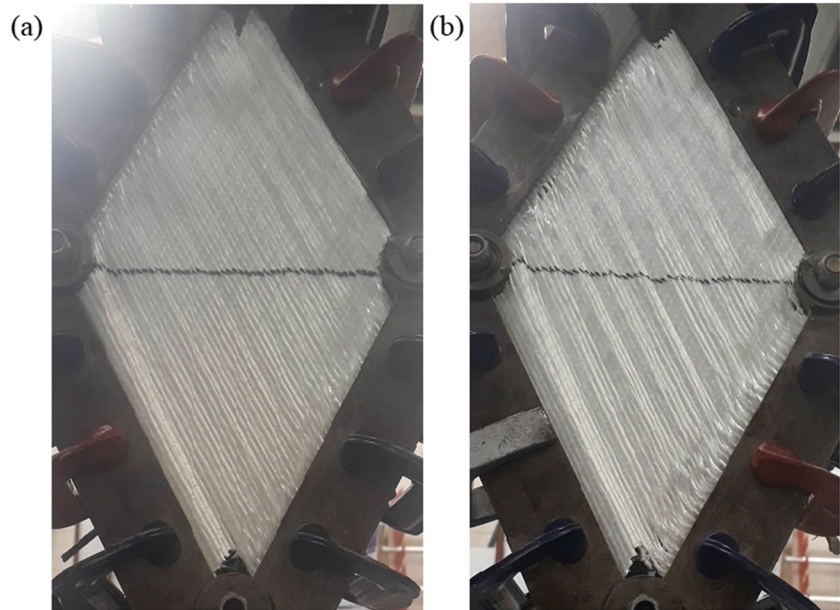

Fig. 14 Wrinkling behaviour of PF test specimens at 30° of shear angles for the: (a) high pressure G-clamped PF test (b) low pressure G-clamped PF test and (c) tightly-clamped 6 mm pre-displaced PF test

therefore result in the measured force being lower than the true signal and represents an opposite (but probably less severe) error than that resulting from fibre tension due to sample misalignment.

When compared to the standard tightly-clamped PF test, both G-clamped test methods (high and low-pressure) show a large reduction in normalised shear force; even the high-pressure G-clamped PF test result is significantly lower than that of the standard tightly-clamped PF test. The standard method prevents slip in the clamping area because the specimen is tightly bolted in the rig (see Fig. 2b). In contrast, in the G-clamped method, the ends of the tows can slip from within the clamps due to the lower clamping pressure and the presence of rubber strips placed on either side of the sample (see Fig. 10b). Therefore, any induced tow tension in the G-clamped test specimens will be more easily dissipated.

The low-pressure G-clamped results have very little additional contribution due to fibre tension (the signal to noise ratio is high). However, wrinkle formation at the early stages of the test may lead to underestimates of the true signal. Therefore, once the specimen begins to wrinkle, the measured force from the low-pressure G-clamped may be less reliable (beyond about 19.4°). In contrast, the high-pressure G-clamped results may contain some additional contribution from fibre tension at low shear angles due to the higher clamping pressure (i.e. the signal to noise ratio is low at small angles), but this tension will be dissipated at higher shear angles due to the greater forces involved in shearing the specimen and the non-rigid boundary condition at the clamps. The measured data in the high-pressure G-clamped is therefore likely to be more reliable at high shear angles as the noise to signal ratio grows relatively large (at least compared to the standard tightly-clamped PF test). One tentative approach might therefore be to combine both high and low-pressure G-clamped data. For example, beyond the wrinkle onset angle of the low-pressure G-clamped PF test, the weighted average of both the low and high-pressure G-clamped PF test results, W, can be calculated using Eq. (8) where, w_L and w_H represent linear weighting function applied to values (i.e., at 19.4° of shear, w_L and w_H are 100 and 0, respectively, and decrease/ increase linearly as they approach the final shear angle of the test measurement), and X_L and X_H are the data values from the low and high G-clamp pressure PF tests, respectively.

$$W = \frac{w_L X_L + w_H X_H}{w_L + w_H} \tag{8}$$

The resulting combined G-clamped test curve (indicated by the black dotted lines in Fig. 12) is almost identical to the 6 mm pre-displaced tightly-clamped PF test result. This could simply be a coincidence, or it could be postulated that using two different approaches to arrive at the same result

provides mutual verification of both methods. To explore this assumption, Fig. 14 compares the wrinkling behaviour of high and low pressure G-clamped PF test specimens, and the 6 mm pre-displaced PF test specimens, all at a 30° shear angle (according to Fig. 12, the 6 mm pre-displaced PF test shows an intermediate force between the high and low pressure G-clamped test curves at 30° shear angle). The wrinkle behaviour (i.e., the amplitude and number of wrinkles) of the 6 mm pre-displaced PF test method lies between the high and low-pressure G-clamped specimens. Therefore, it does seem reasonable to expect that the specimens will behave similarly and produce comparable results during the two different PF test modifications (G-clamped and 6 mm pre-displaced).

Note that PF tests were also performed in the negative bias directions to determine whether shear force depends on the shear direction (relative to the stitching). Due to the symmetric architecture of this UD stitched non-crimp fabric, no significant difference was observed (i.e., average results were present within the ± 1SD—see Fig. 15).

Conclusions

The in-plane shear behaviour of a UD-NCF tricot-chain stitched glass fabric was measured using a Picture Frame test and the Uniaxial Bias Extension test. The normalised force curves of the two standard shear tests initially suggested a significant difference, with the standard tightly-clamped PF test result being dramatically higher than the UBE test result. Conscious of the well-investigated issue regarding the clamping conditions of the PF test [46, 49–54], different simple modifications to the test were made, to determine
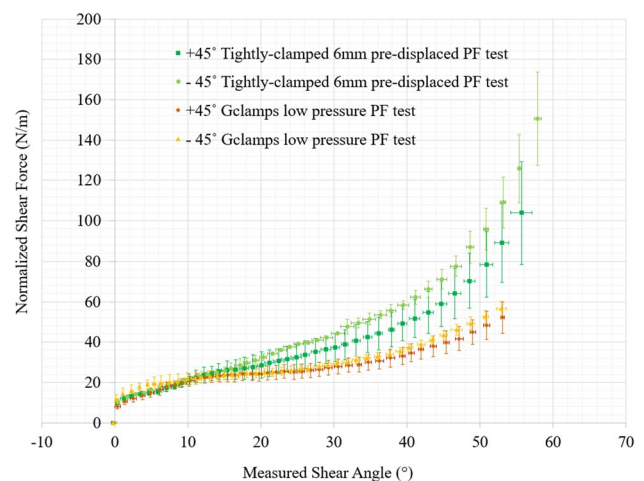

Fig. 15 Comparison of normalized force vs measured shear angle curves of selected PF tests in positive and negative bias directions

whether the higher shear force measured in the standard tightly-clamped PF test for this particular material was reliable or not. Past investigations have devised ingenious new PF rigs with tensioning devises employing needles rather than clamps along the PF edges, to reduce misalignment errors and adjust fibre tension [45, 55]. The aim here is to investigate the boundary condition using a basic PF test rig, mainly because a simple solution is likely to be more accessible to most researchers, but also because the needle-type boundary condition may not be appropriate for fragile UD-NCFs. It is noted however, that the possibility of using a needle-type boundary condition, while more elaborate, could offer another viable alternative and may be something to consider in the future.

Positively pre-displaced tightly-clamped PF testing (a simple modification of the standard tightly-clamped PF test) was performed to minimise fabric tension caused by misalignment. The 6 mm pre-displaced method shows a significant reduction of normalized force compared to the standard tightly-clamped PF test. The reason for this reduction in normalised force is that the tows undergo compressive stresses rather than tension. This is evidenced by the onset of wrinkling at low shear angles.

Another approach for modifying the standard tightly-clamped PF test is the G-clamp method (clamping modification) – similar clamping conditions were used on quasi-UD-NCFs by Schirmaier et al. [9], Ghazimoradi et al. [11] and Senner et al. [40]. This method simplifies specimen preparation by eliminating preparation steps (such as bonding aluminium sheets and drilling of bolt holes) and allows for relatively easy variation of the clamping pressure. The idea is to apply the least clamping pressure possible while still inducing the required kinematics, this philosophy is aligned with the suggestions made in some of the earliest work using PF tests [50, 51], i.e. to use a low clamping pressure rather than a tightly bolted boundary condition [53]. As such, the G-clamp method was performed with two different tightening pressures (low and high) to determine how the clamping condition affected the measured shear force. Based on wrinkling observations, a progressively weighted combination of the two G-clamp PF test results was suggested as an optimum compromise, with the low clamping pressure taking precedence at low shear angles (low forces) and the high clamping pressure taking precedence at high shear angles (high forces). The resulting combined G-clamped PF test curve was almost identical to the 6 mm pre-displaced PF test curve, suggesting that these two distinct approaches may achieve similar results. In practise, the combined (low and high) G-clamped PF test is preferred over the tightly-clamped 6 mm pre-displaced test method because, even though twice the number of the tests need to be performed, the method saves time by simplifying test sample preparation. The use of a tightly clamped (bolted)

boundary condition in a standard PF test [53] i.e. with no pre-displacement, is not recommended, as the potential for error is thought to be too great [46, 49].

This investigation began by postulating that the difference in behaviour in the standard PF test and the UBE test (the standard tightly-clamped PF test result being much higher) could be due to: (*a*) *experimental error* or (*b*) *a real change in shear resistance of the fabric in the two tests*. Following this investigation, it seems reasonable to conclude that the difference is partly due to both these factors. Even after eliminating the misalignment error in the PF test, the normalised force measured in the UBE test is still significantly lower than that measured in the modified PF tests, but the difference is smaller than initially measured (see Fig. 16). The modified PF test result is higher by a factor of 8X at 5°, 4X at 10° and 2X at 30°, whereas the standard tightly-clamped PF test result is higher by a factor of 16X at 5°, 10X at 10° and 3X at 30°. This difference is nevertheless considerable. A possible explanation for the lower measured force in the UBE test is that the observed extension in the stitch direction during the UBE test significantly reduces the fabric's shear resistance. The free edge of the UBE specimen could also lead to decreased shear stiffness as it facilitates some degree of slipping rather than stretching of the stitch, possibly leading to specimen size dependence [40].

Future research plan

To fully characterise the UD-NCFs forming behaviour, new test methods must be introduced to induce well-defined in-plane deformation kinematics with different combinations of
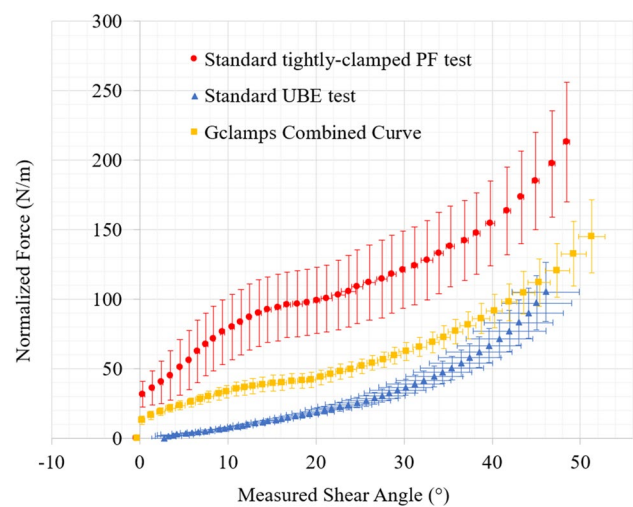

Fig. 16 Comparison of normalized force vs measured shear angle curves of standard tightly-clamped PF test, standard UBE test and resultant G-clamped PF test combined curve

shear and stitch strain. A 3D force surface in (shear angle) vs (stitch tensile strain) parameter space can then be generated by combining the results of each test. The study will provide a method for determining the true forming behaviour of UD-NCFs that have compliant stitching thread and no stabilising transverse glass tows, and the data will be useful in developing associated constitutive models in the future.

Appendix A: Derivation of engineering strain along the fibre direction in the positive pre-displaced PF rig test

Figure 17

Based on the test geometry change, the fabric shear angle (θ) of the standard PF test was derived by directly relating it to the displacement of the crosshead, D. L_{pf} is the side length of the picture frame rig (see Fig. 7 and Eq. (1)).

$$\theta = \frac{\pi}{2} - 2acos\left[\frac{1}{\sqrt{2}} + \frac{D}{2L_{pf}}\right] \qquad (9)$$

The tow-stitch angle of the standard PF test is related to the frame angle of the positive pre-displaced PF test. For a 4 mm pre-displaced PF rig, the initial frame angle θ_1 (see Fig. 17a) can be calculated as,

$$\theta_1 = acos\left[\frac{1}{\sqrt{2}} + \frac{0.004}{2L_{pf}}\right] \qquad (10)$$

Using Fig. 17a, the initial length of the tows (L_1) can be estimated as,
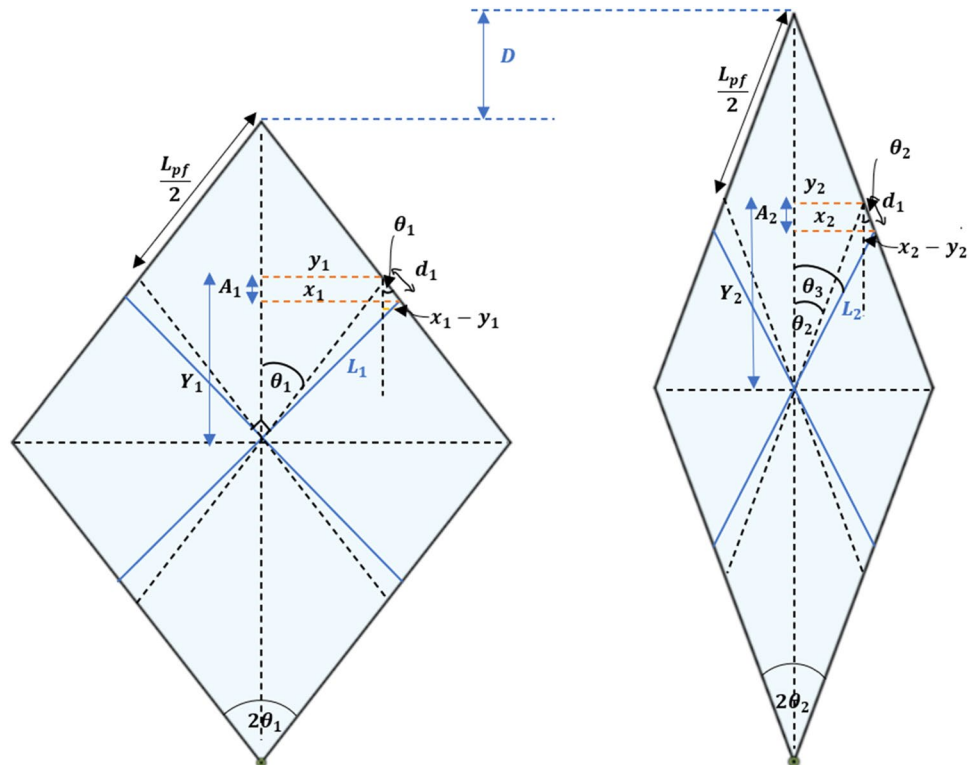
$$L_1 = \sqrt{2}(Y_1 - A_1) \qquad (11)$$

where,

$$Y_1 = \left[\frac{L_{pf}}{2}\right]cos\theta_1 \qquad (12)$$

$$A_1 = \frac{\left[\frac{L_{pf}}{2}\right]cos\theta_1\left(cos\theta_1 - sin\theta_1\right)}{cos\theta_1 + sin\theta_1} \qquad (13)$$

$$\therefore L_1 = \sqrt{2}\left\{\left(\left[\frac{L_{pf}}{2}\right]cos\theta_1\right) - \left(\frac{\left[\frac{L_{pf}}{2}\right]cos\theta_1\left(cos\theta_1 - sin\theta_1\right)}{cos\theta_1 + sin\theta_1}\right)\right\} \qquad (14)$$

The frame angle at a given displacement θ_2 (see Fig. 17b) can be calculated as,

Fig. 17 Positive pre-displaced of the PF rig (**a**) Loaded specimen to the positively pre-displaced rig (**b**) The picture frame rig after crosshead displacement, D

$$\theta_2 = acos\left[\frac{1}{\sqrt{2}} + \frac{D}{2L_{pf}}\right] \tag{15}$$

Using trigonometry,

$$Y_2 = \left[\frac{L_{pf}}{2}\right]\cos\theta_2 \tag{16}$$

$$A_2 = d_1\cos\theta_2 \tag{17}$$

$$x_2 = d_1\sin\theta_2 + \left[\frac{L_{pf}}{2}\right]\sin\theta_2 \tag{18}$$

where

$$d_1 = \frac{A_1}{\cos\theta_1} \tag{19}$$

$$\tan\theta_3 = \frac{x_2}{Y_2 - A_2} \tag{20}$$

By applying Eq. (16), (17) and (18) to Eq. (20) the tow-stitch angle, θ_3, at a given displacement can be calculated as

$$\theta_3 = \tan^{-1}\left[\frac{(\tan\theta_2)(2d_1 + L_{pf})}{L_{pf} - 2d_1}\right] \tag{21}$$

Therefore, the theoretical length of the tows at a given displacement, L_2, can be estimated as,

$$L_2 = \frac{x_2}{\sin\theta_3} \tag{22}$$

Apply Eq. (18) and Eq. (21) to Eq. (22).

$$L_2 = \frac{\left(d_1\sin\theta_2 + \left[\frac{L_{pf}}{2}\right]\sin\theta_2\right)}{\sin\left(\tan^{-1}\left[\frac{(\tan\theta_2)(2d_1 + L_{pf})}{L_{pf} - 2d_1}\right]\right)} \tag{23}$$

The engineering strain of the tows (ε_p) in the positive pre-displaced PF rig test is given in Eq. (24)

$$\varepsilon_p = \frac{L_2 - L_1}{L_1} \tag{24}$$

By applying Eq. (14) and Eq. (23) to Eq. (24), the theoretical engineering strain of the tows in the positive pre-displaced PF rig test at a given displacement can be calculated as,

$$\varepsilon_p = \frac{\left\{\frac{d_1\sin\theta_2 + \left[\frac{L_{pf}}{2}\right]\sin\theta_2}{\sin\left(\tan^{-1}\left[\frac{(\tan\theta_2)(2d_1 + L_{pf})}{L_{pf} - 2d_1}\right]\right)}\right\} - \left\{\sqrt{2}\left(\left[\frac{L_{pf}}{2}\right]\cos\theta_1 - \frac{\left[\frac{L_{pf}}{2}\right]\cos\theta_1(\cos\theta_1 - \sin\theta_1)}{\cos\theta_1 + \sin\theta_1}\right)\right\}}{\left\{\sqrt{2}\left(\left[\frac{L_{pf}}{2}\right]\cos\theta_1 - \frac{\left[\frac{L_{pf}}{2}\right]\cos\theta_1(\cos\theta_1 - \sin\theta_1)}{\cos\theta_1 + \sin\theta_1}\right)\right\}}$$

Appendix B: Derivation of the theoretical shear angle in the positive pre-displaced PF rig test

Substituting Eq. (15) in Eq. (21)

$$\theta_3 = \tan^{-1}\left\{\frac{tan\left(acos\left[\frac{1}{\sqrt{2}} + \frac{D}{2L_{pf}}\right]\right)(2d_1 + L_{pf})}{L_{pf} - 2d_1}\right\} \tag{25}$$

θ_3 represents half of the tow-stitch angle at a given displacement. The theoretical shear angle of the positive pre-displaced PF test (δ_p) can be calculated by applying Eq. (25) to Eq. (9)

$$\theta = \frac{\pi}{2} - 2acos\left[\frac{1}{\sqrt{2}} + \frac{D}{2L_{pf}}\right]$$

$$\delta_p = \frac{\pi}{2} - 2\tan^{-1}\left\{\frac{tan\left(acos\left[\frac{1}{\sqrt{2}} + \frac{D}{2L_{pf}}\right]\right)(2d_1 + L_{pf})}{L_{pf} - 2d_1}\right\}$$

Appendix C: Derivation of engineering strain along fibre direction of the negative pre-displaced PF rig test

Figure 18

The tow-stitch angle of the standard PF test is related to the frame angle of the negative pre-displaced PF test.

$$\theta = \frac{\pi}{2} - 2acos\left[\frac{1}{\sqrt{2}} - \frac{D}{2L_{pf}}\right] \tag{26}$$

For a 4 mm negative pre-displaced PF rig, the initial frame angle θ_1 (see Fig. 18a) can be calculated as,

$$\therefore \theta_1 = acos\left[\frac{1}{\sqrt{2}} - \frac{0.004}{2L_{pf}}\right] \tag{27}$$

Fig. 18 Negative pre-displaced of the PF rig (**a**) Loaded specimen to the negative pre-displaced rig (**b**) The picture frame rig after crosshead displacement, D
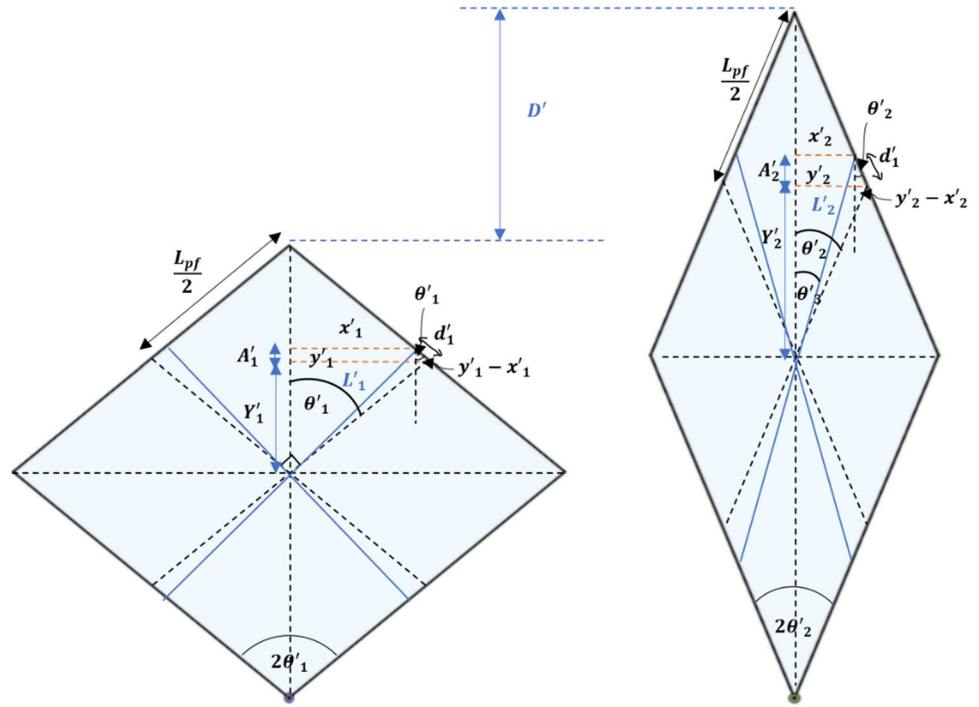
Using Fig. 18a, the initial length of the tows (L_1') can be estimated as,

$$L_1' = \sqrt{2}(Y_1' + A_1') \tag{28}$$

where,

$$Y_1' = \left[\frac{L_{pf}}{2}\right]\cos\theta_1' \tag{29}$$

$$A_1' = \frac{\left[\frac{L_{pf}}{2}\right]\cos\theta_1'\left(\sin\theta_1' - \cos\theta_1'\right)}{\sin\theta_1' + \cos\theta_1'} \tag{30}$$

$$Y_2' = \left[\frac{L_{pf}}{2}\right]\cos\theta_2' \tag{33}$$

$$A_2' = d_1'\cos\theta_2' \tag{34}$$

$$x_2' = \left[\frac{L_{pf}}{2}\right]\sin\theta_2' - d_1'\sin\theta_2' \quad (35\text{0where}$$

$$d_1' = \frac{A_2'}{\cos\theta_2'} \tag{35}$$

$$\tan\theta_3' = \frac{x_2'}{Y_2' + A_2'} \tag{36}$$

$$\therefore L_1' = \sqrt{2}\left\{\left(\left[\frac{L_{pf}}{2}\right]\cos\theta_1'\right) + \left(\frac{\left[\frac{L_{pf}}{2}\right]\cos\theta_1'\left(\sin\theta_1' - \cos\theta_1'\right)}{\sin\theta_1' + \cos\theta_1'}\right)\right\} \tag{31}$$

The frame angle at a given displacement θ_2' (see Fig. 18b) can be calculated as,

$$\theta_2' = a\cos\left[\frac{1}{\sqrt{2}} + \frac{D'}{2L_{pf}}\right] \tag{32}$$

Using trigonometry,

By applying Eq. (33), (34) and (35) to Eq. (37) the tow-stitch angle, θ_3', at a given displacement can be calculated as,

$$\theta_3' = \tan^{-1}\left[\frac{\left(\tan\theta_2'\right)\left(L_{pf} - 2d_1'\right)}{L_{pf} + 2d_1'}\right] \tag{37}$$

Therefore, the theoretical length of the tows at a given displacement, L_2' can be estimated as,

$$L_2' = \frac{x_2'}{\sin\theta_3'} \tag{38}$$

Apply Eq. (35) and Eq. (38) to Eq. (39).

$$L_2' = \frac{\left(\left[\frac{L_{pf}}{2}\right]\sin\theta_2' - d_1'\sin\theta_2'\right)}{\sin\left(\tan^{-1}\left[\frac{(\tan\theta_2')(L_{pf}-2d_1')}{L_{pf}+2d_1'}\right]\right)} \tag{39}$$

The engineering strain of the tows (ε_n) in the negative pre-displaced PF rig test is given in Eq. (41)

$$\varepsilon_n = \frac{L_2' - L_1'}{L_1'} \tag{40}$$

By applying Eq. (31) and Eq. (40) to Eq. (41), the theoretical engineering strain of the tows in the negative pre-displaced PF rig test at a given displacement can be calculated as,

$$\varepsilon_n = \frac{\left\{\frac{\left(\left[\frac{L_{pf}}{2}\right]\sin\theta_2' - d_1'\sin\theta_2'\right)}{\sin\left(\tan^{-1}\left[\frac{(\tan\theta_2')(L_{pf}-2d_1')}{L_{pf}+2d_1'}\right]\right)}\right\} - \left\{\sqrt{2}\left(\left[\frac{L_{pf}}{2}\right]\cos\theta_1' + \frac{\left[\frac{L_{pf}}{2}\right]\cos\theta_1'(\sin\theta_1'-\cos\theta_1')}{\sin\theta_1'+\cos\theta_1'}\right)\right\}}{\left(\sqrt{2}\left(\left[\frac{L_{pf}}{2}\right]\cos\theta_1 - \frac{\left[\frac{L_{pf}}{2}\right]\cos\theta_1(\cos\theta_1-\sin\theta_1)}{\cos\theta_1+\sin\theta_1}\right)\right)}$$

Appendix D: Derivation of the theoretical shear angle of the negative pre-displaced PF test

Substituting Eq. (32) in Eq. (38)

$$\theta_3' = \tan^{-1}\left\{\frac{\tan\left(acos\left[\frac{1}{\sqrt{2}} + \frac{D'}{2L_{pf}}\right]\right)(L_{pf} - 2d_1')}{L_{pf} + 2d_1'}\right\} \tag{41}$$

θ_3' represents half of the tow-stitch angle at a given displacement. The theoretical shear angle of the negative pre-displaced PF test (δ_n) can be calculated as,

$$\delta_n = \frac{\pi}{2} - 2\tan^{-1}\left\{\frac{\tan\left(acos\left[\frac{1}{\sqrt{2}} + \frac{D'}{2L_{pf}}\right]\right)(L_{pf} - 2d_1')}{L_{pf} + 2d_1'}\right\}$$

Declarations

Ethical statement The submission contains original research work and has been approved by all authors. The work presented in the manuscript has not been published previously.

Conflict of interest The authors declare that they have no conflict of interest.

References

1. Loos M (2014) Carbon nanotube reinforced composites: CNT Polymer Science and Technology. Elsevier. https://doi.org/10.1016/C2012-0-06123-6

2. Shipsha A, Hallström S, Burman M (2019) Effect of stacking sequence and bundle waviness in quasi-isotropic NCF composites subjected to compression. Compos Part B Eng 178:107423. https://doi.org/10.1016/j.compositesb.2019.107423

3. Chen S, Joesbury AM, Yu F, Harper LT, Warrior NA (2022) Optimisation of intra-ply stitch removal for improved formability of biaxial non-crimp fabrics. Compos Part B Eng 229:109464. https://doi.org/10.1016/j.compositesb.2021.109464

4. Colin D, Bel S, Hans T, Hartmann M, Drechsler K (2020) Virtual Description of Non-Crimp Fabrics at the Scale of Filaments Including Orientation Variability in the Fibrous Layers. Appl Compos Mater 27(4):337–355. https://doi.org/10.1007/s10443-020-09819-1

5. Vallons K (2009) The Behaviour of Carbon Fibre - Epoxy NCF Composites under Various Mechanical Loading Conditions. Dissertation, Catholic University of Leuven. https://www.researchgate.net/publication/235976998_The_Behaviour_of_Carbon_Fibre_-_Epoxy_NCF_Composites_under_Various_Mechanical_Loading_Conditions

6. Sandoval EAT (2020) Characterizing the deformation response of a unidirectional non-crimp fabric for the development of computational draping simulation models. Dissertation, University of Waterloo. https://uwspace.uwaterloo.ca/bitstream/handle/10012/15974/TrejoSandoval_EleazarAlberto.pdf?sequence=3&isAllowed=y

7. Jiang G, Gao Z, Ma P, Miao X, Zhu Y (2014) Comparative study on the mechanical behavior of carbon weft-knitted biaxial fabrics stitched by polyester fibers and preoxidized polyacrylonitrile fibers. J Ind Text 44(1):5–21. https://doi.org/10.1177/1528083713518086

8. Wouters M (2002) Effects of fibre bundle size and stitch pattern on the static properties of unidirectional carbon-fibre non-crimp fabric composites. Dissertation, Lulea University of

Technology. https://www.diva-portal.org/smash/get/diva2:101679 9/FULLTEXT01.pdf

9. Schirmaier FJ, Weidenmann KA, Kärger L, Henning F (2016) Characterisation of the draping behaviour of unidirectional non-crimp fabrics (UD-NCF). Compos Part A Appl Sci Manuf 80:28–38. https://doi.org/10.1016/j.compositesa.2015.10.004

10. Harrison P, Härtel F (2014) Evaluation of normalisation methods for uniaxial bias extension tests on engineering fabrics. Compos Part A Appl Sci Manuf 67:61–69. https://doi.org/10.1016/j.compositesa.2014.08.011

11. Ghazimoradi M, Trejo EA, Carvelli V, Butcher C, Montesano J (2021) Deformation characteristics and formability of a tricot-stitched carbon fiber unidirectional non-crimp fabric. Compos Part A Appl Sci Manuf 145:106366. https://doi.org/10.1016/j.compositesa.2021.106366

12. Lomov SV (ed) (2011) Non-crimp fabric composites: manufacturing, properties, and applications. Cambridge, Woodhead Publisher Ltd

13. Heß H, Himmel N (2011) Structurally stitched NCF CFRP laminates. Part 1: Experimental characterization of in-plane and out-of-plane properties. Compos Sci Technol 71(5):549–568. https://doi.org/10.1016/j.compscitech.2010.11.012

14. Beier U, Fischer F, Sandler JK, Altstädt V, Weimer C, Spanner H, Buchs W (2008) Evaluation of preforms stitched with a low melting-temperature thermoplastic yarn in carbon fibre-reinforced composites. Compos Part A Appl Sci Manuf 39(5):705–711. https://doi.org/10.1016/j.compositesa.2008.02.011

15. Hashmi MSJ (2014) Comprehensive materials processing. Newnes

16. Ouagne P, Soulat D, Moothoo J, Capelle E, Gueret S (2013) Complex shape forming of a flax woven fabric; analysis of the tow buckling and misalignment defect. Compos Part A Appl Sci Manuf 51:1–10. https://doi.org/10.1016/j.compositesa.2013.03.017

17. Goergen C, Baz S, Mitschang P, Gresser GT (2017) Recycled carbon fibers in complex structural parts-organic sheets made of rCF staple fiber yarns In: Key Engineering Materials. Trans Tech Publications Ltd 742:602–609. https://doi.org/10.4028/www.scientific.net/KEM.742.602

18. Chen H, Li S, Wang J, Ding A (2021) A focused review on the thermo-stamping process and simulation progresses of continuous fibre reinforced thermoplastic composites. Compos Part B Eng 224:109196. https://doi.org/10.1016/j.compositesb.2021.109196

19. Hallander P, Sjölander J, Åkermo M (2015) Forming induced wrinkling of composite laminates with mixed ply material properties; an experimental study. Compos Part A Appl Sci Manuf 78:234–245. https://doi.org/10.1016/j.compositesa.2015.08.025

20. Boisse P, Hamila N, Vidal-Sallé E, Dumont F (2011) Simulation of wrinkling during textile composite reinforcement forming. Influence of tensile, in-plane shear and bending stiffnesses. Compos Sci Technol 71(5):683–692. https://doi.org/10.1016/j.compscitech.2011.01.011

21. Fu Y, Yao X (2022) A review on manufacturing defects and their detection of fiber reinforced resin matrix composites. Composites Part C: Open Access 8:100276. https://doi.org/10.1016/j.jcomc.2022.100276

22. Harrison P, Gomes R, Curado-Correia N (2013) Press forming a 0/90 cross-ply advanced thermoplastic composite using the double-dome benchmark geometry. Compos Part A Appl Sci Manuf 54:56–69. https://doi.org/10.1016/j.compositesa.2013.06.014

23. Coffin DW, Pipes RB (2004) Flange Wrinkling in The Forming of Thermoplastic Composite Sheets. In: AIP Conference Proceedings. Am Instit Phys 712(1):294–299. https://doi.org/10.1063/1.1766539

24. Harrison P (2016) Modelling the forming mechanics of engineering fabrics using a mutually constrained pantographic beam and membrane mesh. Compos Part A Appl Sci Manuf 81:145–157. https://doi.org/10.1016/j.compositesa.2015.11.005

25. Giorgio I, Harrison P, Dell'Isola F, Alsayednoor J, Turco E (2018) Wrinkling in engineering fabrics: a comparison between two different comprehensive modelling approaches. Proc Royal Soc A: Mathematical, Physical and Engineering Sciences 474(2216):20180063. https://doi.org/10.1098/rspa.2018.0063

26. Abdiwi F, Harrison P, Yu WR (2013) Modelling the shear-tension coupling of woven engineering fabrics. Adv Mater Sci Eng 2013 https://doi.org/10.1155/2013/786769

27. Harrison P, Alvarez MF, Anderson D (2018) Towards comprehensive characterisation and modelling of the forming and wrinkling mechanics of engineering fabrics. Int J Solids Struct 154:2–18. https://doi.org/10.1016/j.ijsolstr.2016.11.008

28. Potluri P, Ciurezu DP, Ramgulam RB (2006) Measurement of meso-scale shear deformations for modelling textile composites. Compos Part A Appl Sci Manuf 37(2):303–314. https://doi.org/10.1016/j.compositesa.2005.03.032

29. Harrison P, Abdiwi F, Guo Z, Potluri P, Yu WR (2012) Characterising the shear–tension coupling and wrinkling behaviour of woven engineering fabrics. Compos Part A Appl Sci Manuf 43(6):903–914. https://doi.org/10.1016/j.compositesa.2012.01.024

30. Harrison P, Curado-Correia N (2013) Temperature and rate dependent multi-scale shear modelling of molten thermoplastic advanced composties. In: 19th International Conference on Composite Materials. Montreal, Canada. https://eprints.gla.ac.uk/85556/

31. Hsiao SW, Kikuchi N (1999) Numerical analysis and optimal design of composite thermoforming process. Comput Methods Appl Mech Eng 177(1–2):1–34. https://doi.org/10.1016/S0045-7825(98)00273-4

32. Wang J, Wang P, Hamila N, Boisse P (2020) Mesoscopic analyses of the draping of 3D woven composite reinforcements based on macroscopic simulations. Compos Struct 250:112602. https://doi.org/10.1016/j.compstruct.2020.112602

33. Schirmaier FJ, Dörr D, Henning F, Kärger L (2017) A macroscopic approach to simulate the forming behaviour of stitched unidirectional non-crimp fabrics (UD-NCF). Compos Part A Appl Sci Manuf 102:322–335. https://doi.org/10.1016/j.compositesa.2017.08.009

34. Ghazimoradi M, Trejo EA, Butcher C, Montesano J (2022) Characterizing the macroscopic response and local deformation mechanisms of a unidirectional non-crimp fabric. Compos Part A Appl Sci Manuf 156:106857. https://doi.org/10.1016/j.compositesa.2022.106857

35. Krogh C, Kepler JA, Jakobsen J (2021) Pure and simple: investigating the in-plane shear kinematics of a quasi-unidirectional glass fiber non-crimp fabric using the bias-extension test. Int J Mater Form 14(6):1483–1495. https://doi.org/10.1007/s12289-021-01642-8

36. Trejo EA, Ghazimoradi M, Butcher C, Montesano J (2020) Assessing strain fields in unbalanced unidirectional non-crimp fabrics. Compos Part A Appl Sci Manuf 130:105758. https://doi.org/10.1016/j.compositesa.2019.105758

37. Habboush A, Sanbhal N, Shao H, Jiang J, Chen N (2018) Characterization and analysis of in-plane shear behavior of glass warp-knitted non-crimp fabrics based on picture frame method. Materials 11(9):1550. https://doi.org/10.3390/ma11091550

38. Habboush A, Sanbhal N, Shao H, Jiang J, Chen N (2020) Characterization and analysis of wrinkling behavior of glass warp knitted non-crimp fabrics based on double-dome draping geometry. J Eng Fibers Fabr 15:1–17. https://doi.org/10.1177/1558925020958521

39. Vallons K, Adolphs G, Lucas P, Lomov SV, Verpoest I (2013) Quasi-UD glass fibre NCF composites for wind energy

applications: a review of requirements and existing fatigue data for blade materials. Mech Ind 14(3):175–189. https://doi.org/10.1051/meca/2013045

40. Senner T, Kreissl S, Merklein M, Meinhardt J, Lipp A (2014) A modular modeling approach for describing the in-plane forming behavior of unidirectional non-crimp-fabrics. Prod Eng 8:635–643. https://doi.org/10.1007/s11740-014-0561-z

41. Bhat S, Dittel G, Knobel A, Gries T (2022) Investigation of the drapability of elastic-adapted textile reinforcements for double-curved concrete panels. In: SAMPE EUROPE Conference and Exhibition 2022. Hamburg, Germany

42. Viisainen J (2022) Wrinkling behaviour of biaxial non-crimp fabrics during preforming Dissertation, University of Cambridge https://doi.org/10.17863/CAM.81052

43. Rueden C, Dietz C, Horn M, Schindelin J, Northan B, Berthold M, Eliceiri K (2016) ImageJ Ops [Software], [Online] Available: https://imagej.net/Ops

44. Harrison P, Clifford MJ, Long AC (2004) Shear characterisation of viscous woven textile composites: a comparison between picture frame and bias extension experiments. Compos Sci Technol 64(10–11):1453–1465. https://doi.org/10.1016/j.compscitech.2003.10.015

45. Launay J, Hivet G, Duong AV, Boisse P (2008) Experimental analysis of the influence of tensions on in plane shear behaviour of woven composite reinforcements. Compos Sci Technol 68(2):506–515. https://doi.org/10.1016/j.compscitech.2007.06.021

46. Lebrun G, Bureau MN, Denault J (2003) Evaluation of bias-extension and picture-frame test methods for the measurement of intraply shear properties of PP/glass commingled fabrics. Compos Struct 61(4):341–352. https://doi.org/10.1016/S0263-8223(03)00057-6

47. Harrison P (2012) Normalisation of biaxial bias extension test results considering shear tension coupling. Compos Part A Appl Sci Manuf 43(9):1546–1554. https://doi.org/10.1016/j.compositesa.2012.04.014

48. Harrison P, Wiggers J, Long AC (2008) Normalisation of Shear Test Data for Rate-Independent Compressible Fabrics. J Compos Mater 42(22):2315–2344. https://doi.org/10.1177/0021998308095367

49. Milani AS, Nemes JA, Lebrun G, Bureau MN (2010) A comparative analysis of a modified picture frame test for characterization of woven fabrics. Polym Compos 31(4):561–568. https://doi.org/10.1002/pc.20849

50. McGuinness GB, ÓBrádaigh CM, (1997) Development of rheological models for forming flows and picture-frame shear testing of fabric reinforced thermoplastic sheets. J Nonnewton Fluid Mech 73:1–28. https://doi.org/10.1016/S0377-0257(97)00040-2

51. McGuinness GB, ÓBrádaigh CM (1998) Characterisation of thermoplastic composite melts in rhombus-shear: the picture-frame experiment". Compos Part A Appl Sci Manuf 29:115–132. https://doi.org/10.1016/S1359-835X(97)00061-4

52. Hivet G, Duong AV (2011) A contribution to the analysis of the intrinsic shear behavior of fabrics. J Compos Mater 45(6):695–716. https://doi.org/10.1177/0021998310382315

53. Cao J, Akkerman R, Boisse P, Chen J, Cheng HS, de Graaf EF, Gorczyca JL, Harrison P, Hivet G, Launay J, Lee W, Liu L, Lomov SV, Long A, de Luycker E, Morestin F, Padvoiskis J, Peng XQ, Sherwood J, Tz S, Tao XM, Verpoest I, Willems A, Wiggers J, Yu TX, Zhu B (2008) Characterization of mechanical behavior of woven fabrics: experimental methods and benchmark results. Compos Part A Appl Sci Manuf 39(6):1037–1053. https://doi.org/10.1016/j.compositesa.2008.02.016

54. Lomov SV, Boisse P, Deluycker E, Morestin F, Vanclooster K, Vandepitte D, Verpoest I, Willems A (2008) Full-field strain measurements in textile deformability studies. Compos Part A Appl Sci Manuf 39(8):1232–1244. https://doi.org/10.1016/j.compositesa.2007.09.014

55. Hosseini A, Kashani MH, Sassani F, Milani AS, Ko FK (2018) Identifying the distinct shear wrinkling behavior of woven composite preforms under bias extension and picture frame tests. Compos Struct 185:764–773. https://doi.org/10.1016/j.compstruct.2017.11.033

56. Nosrat-Nezami F, Gereke T, Eberdt C, Cherif C (2014) Characterisation of the shear–tension coupling of carbon-fibre fabric under controlled membrane tensions for precise simulative predictions of industrial preforming processes. Compos Part A Appl Sci Manuf 67:131–139. https://doi.org/10.1016/j.compositesa.2014.08.030

57. Li L, Zhao Y, Chen Y, Yang J, Duan Y (2014) In-plane shear investigation of biaxial carbon non-crimp fabrics with experimental tests and finite element modeling. Mater Des 63:757–765. https://doi.org/10.1016/j.matdes.2014.07.007

58. Montazerian H, Rashidi A, Hoorfar M, Milani AS (2019) A frameless picture frame test with embedded sensor: Mitigation of imperfections in shear characterization of woven fabrics. Compos Struct 211:112–124. https://doi.org/10.1016/j.compstruct.2018.11.096

59. Pickett AK (2021) Introduction to Process and Mechanical Modelling of Engineering Composites Part 1 Fundamentals. University Stuttgart, Germany

60. Krishnappa L, Ohlendorf JH, Brink M, Thoben KD (2021) Investigating the factors influencing the shear behaviour of 0/90° non-crimp fabrics to form a reference shear test. J Compos Mater 55(20):2739–2750. https://doi.org/10.1177/0021998321991625

61. Clifford MJ, Long AC, De Luca P (2001) Forming of engineered prepregs and reinforced thermoplastics. In: Second Global Symposium on Innovations in Materials Processing and Manufacturing: Sheet Materials, New Orleans, US, pp 303–316. https://scholar.google.com/citations?view_op=view_citation&hl=fr&user=tP-ZEB0AAAAJ&citation_for_view=tP-ZEB0AAAAJ:WF5omc3nYNoC

62. Alsayednoor J, Lennard F, Yu WR, Harrison P (2017) Influence of specimen pre-shear and wrinkling on the accuracy of uniaxial bias extension test results. Compos Part A Appl Sci Manuf 101:81–97. https://doi.org/10.1016/j.compositesa.2017.06.006

63. Lee A (2013) VitualDub 1.10.4.0. [software], [Online] Available: http://www.virtualdub.org